

IRIS: A Real-World Benchmark for Inverse Recovery and Identification of Physical Dynamic Systems from Monocular Video

Rasul Khanbayov^{1*}, Mohamed Rayan Barhdadi^{2*},
Erchin Serpedin², and Hasan Kurban¹

¹ Hamad Bin Khalifa University

² Texas A&M University

🌐 Project Page: <https://iris-benchmark.github.io>

👤 Dataset: <https://huggingface.co/datasets/rasulkhanbayov/IRIS/>

Abstract. Unsupervised physical parameter estimation from video lacks a common benchmark: existing methods evaluate on non-overlapping synthetic data, the sole real-world dataset is restricted to single-body systems, and no established protocol addresses governing-equation identification. This work introduces IRIS, a high-fidelity benchmark comprising 220 real-world videos captured at 4K resolution and 60 fps, spanning both single- and multi-body dynamics with independently measured ground-truth parameters and uncertainty estimates. Each dynamical system is recorded under controlled laboratory conditions and paired with its governing equations, enabling principled evaluation. A standardized evaluation protocol is defined encompassing parameter accuracy, identifiability, extrapolation, robustness, and governing-equation selection. Multiple baselines are evaluated, including a multi-step physics loss formulation and four complementary equation-identification strategies (VLM temporal reasoning, describe-then-classify prompting, CNN-based classification, and path-based labelling), establishing reference performance across all IRIS scenarios and exposing systematic failure modes that motivate future research. The dataset, annotations, evaluation toolkit, and all baseline implementations are publicly released.

Keywords: Physics-based vision, physical parameter estimation, video understanding, benchmark dataset, dynamical systems, governing equation identification

1 Introduction

Extracting physical parameters from video observations constitutes a fundamental inverse problem in computational science, with applications spanning trajectory prediction, biological system characterization, and physical model validation [1–4]. Although recent unsupervised methods have demonstrated encouraging results in

*Equal contribution. Contact: rkhanbayov@hbku.edu.qa, rayan.barhdadi@tamu.edu, and hkurban@hbku.edu.qa

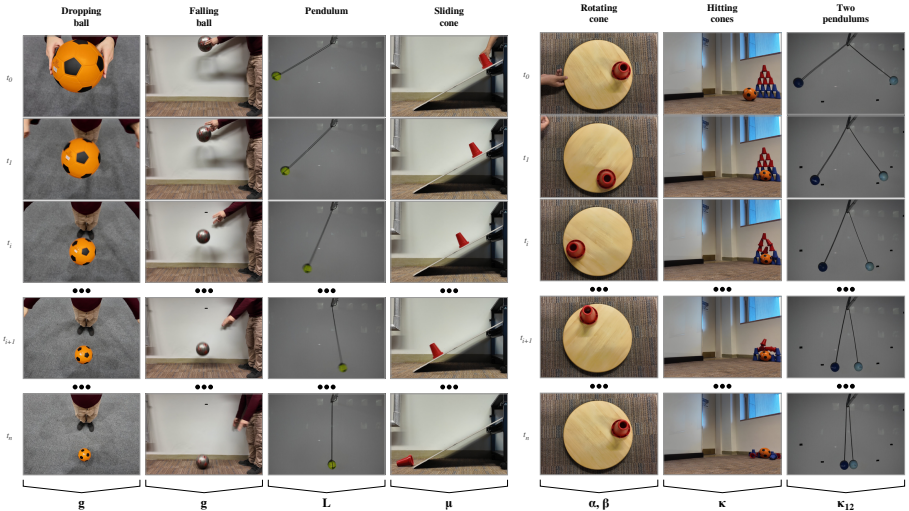


Fig. 1: **Overview of the IRIS benchmark.** Each column corresponds to one of the eight dynamical phenomena; rows show temporally ordered frames sampled from a representative video clip. *Left*: single-body phenomena, including dropping ball, falling ball, pendulum, and sliding cone. *Right*: phenomena unique to IRIS, including rotating cone, hitting cones, and two pendulums. The bottom row indicates the physical parameters targeted for estimation. All videos are recorded at 4K resolution and 60 fps under controlled laboratory conditions with independently measured ground-truth parameters.

estimating parameters of known governing equations from video [2, 3], progress is constrained by the absence of diverse, high-fidelity, real-world benchmark datasets capable of supporting rigorous evaluation and systematic comparison. Existing datasets suffer from several compounding limitations. The majority of prior work evaluates on purely synthetic data, where objects appear in controlled colors against black backgrounds [3, 5, 6]. The sole notable real-world dataset, Delfys75 [7], provides 75 videos at 1920×1080 resolution across five dynamical systems but covers only single-body dynamics, omitting the multi-body collision phenomena central to classical mechanics. No existing benchmark includes scenarios in which physical objects collide and transfer momentum, leaving a significant blind spot in evaluating method capabilities.

These gaps are addressed by IRIS (Interaction and Real-world Inverse physics Sequences), a 4K-resolution dataset designed as a rigorous benchmark for unsupervised physical parameter estimation from video. IRIS retains and extends the single-body scenarios of prior work (dropping ball, falling ball, sliding cone, and pendulum) while introducing three novel multi-body interaction scenarios: a ball striking a pyramid of cones (hitting_cones), two pendulums released simultaneously that collide and dissipate (two_moving_pendulum), and a static pendulum struck by a moving one (two_moving_pendulum_one.static). These

scenarios test recovery of momentum transfer, contact forces, and coupled dynamics, phenomena entirely absent from prior benchmarks. Beyond the dataset itself, a standardized evaluation protocol advances over the Delfys75 baseline along multiple dimensions. First, evaluation axes are formally defined covering parameter accuracy, governing-equation selection, identifiability, robustness, and extrapolation. Second, four complementary equation-identification strategies are benchmarked, providing the first systematic comparison of automatic equation routing for physics identification. Third, a multi-step physics loss formulation is evaluated as a baseline enhancement. Fourth, baseline evaluation on IRIS exposes a critical gradient-flow bug in the state-of-the-art latent-space pipeline [7], demonstrating the diagnostic value of rigorous benchmarking.

The principal contributions are:

IRIS benchmark dataset: A 4K real-world dataset comprising eight dynamical systems, including three novel multi-body interaction scenarios, with independently measured ground-truth parameters and per-setting uncertainty estimates.

Standardized evaluation protocol: A comprehensive framework with five formally defined axes (parameter accuracy, equation selection, identifiability, robustness, extrapolation) and fixed train-per-clip procedures enabling fair benchmarking.

Equation-identification benchmark: The first systematic comparison of four equation-routing strategies, revealing that the ranking of VLM strategies reverses across benchmarks: temporal reasoning leads on Delfys75 (73.33%) while describe-then-classify leads on IRIS (72.92%), and CNN classifiers attain near-perfect in-distribution accuracy (99.30%) but cannot generalize to unseen phenomena.

Multi-step loss baseline and diagnostic findings: A multi-step rollout loss yielding improvements on selected single-body phenomena while exposing catastrophic instabilities on multi-body dynamics.

2 Related Work

2.1 Physical Parameter Estimation from Video

Estimating physical parameters from video constitutes an inverse problem approached through both supervised and unsupervised paradigms. Supervised methods [5, 8–13] achieve strong performance at the cost of requiring labelled datasets that are expensive and frequently infeasible to collect [14]. Unsupervised approaches embed known governing equations within learned latent representations, employing frame reconstruction as a proxy training signal. PAIG [3] integrates a variational autoencoder with a physics engine in the latent space, enabling future frame prediction via a spatial transformer. NIRPI [2] employs a differentiable ODE solver operating at the pixel level, though it requires ground-truth object masks during training. Both rely on frame reconstruction, which constrains the model to roto-translational motion dynamics. A complementary line of research

focuses on learning dynamics models with physics-informed inductive biases. Neural ODEs [15] provide a general framework for continuous-time dynamics. Hamiltonian Neural Networks [16] and Lagrangian Neural Networks [17] enforce energy conservation, while graph neural network-based simulators [18, 19] learn message-passing dynamics for multi-body systems. These operate on state-space inputs rather than raw pixels. Garcia et al. [7] replace frame reconstruction with a latent-space loss combining mean squared error and KL-divergence. However, their pipeline requires the governing equation family to be specified manually, and as identified through our baseline evaluation, contains a critical gradient-flow bug that prevents physics parameters from receiving gradient updates during training.

2.2 Video Benchmarks for Physical Understanding

The majority of existing methods are evaluated on synthetic datasets [3, 5, 6, 9, 12, 13]. Physics101 [20] provides real-world recordings but lacks ground-truth parameters. VideoPhy [21] and Physics-IQ [22] evaluate physical plausibility in generative models rather than quantitative parameter estimation. Delfys75 [7] is the first real-world dataset for unsupervised parameter estimation with ground-truth annotations, but is restricted to single-body dynamics. Recent benchmarks including Morpheus [23], RBench [24], and WorldLens [25] evaluate qualitative physical plausibility rather than quantitative parameter estimation. IRIS is complementary: it targets inverse recovery of continuous physical parameters with ground-truth supervision.

2.3 Vision-Language Models for Physical Reasoning

Large VLMs have demonstrated strong capabilities in visual scene understanding [26–28]. Recent work has explored VLMs for physical reasoning: VideoPhy [21] fine-tunes VLM-based evaluators for physical law adherence, Physics Context Builders [29] produce structured physical scene descriptions, and VLMs have been applied to hypothesize governing functional forms [30]. Despite these advances, the application of VLMs to governing-equation identification for quantitative parameter estimation remains unexplored. IRIS benchmarks four complementary routing strategies for the first time.

2.4 Governing Equation Discovery

SINDy [1] formulates equation discovery as sparse regression over candidate functions, with extensions to latent representations [31]. Symbolic regression methods [4] search expression spaces for closed-form laws, and multimodal LLMs have been applied to discover equations from video [32]. These methods require direct state measurements or high-quality latent representations. IRIS adopts a fixed ODE bank and benchmarks equation-family selection and parameter estimation as separable axes.

2.5 Differentiable Contact and Rigid-Body Simulation

Differentiable physics simulators that learn contact dynamics have advanced rapidly. ContactGaussian-WM [33] combines 3D Gaussian splatting with a differentiable world model, while DiffSim [34] and related work [35, 36] enable gradient-based optimization through differentiable simulation. These approaches model contact explicitly through complementarity or penalty-based formulations, in contrast to the simplified coupling coefficient κ_{ij} employed in the IRIS ODE bank. Adapting such methods to monocular video and evaluating them on IRIS multi-body scenarios is a natural direction for future work.

2.6 Latent ODE Stabilization

The multi-step rollout instability observed on IRIS multi-body dynamics (Sec. 6.3) relates to a broader challenge in training latent ODEs over long horizons. Proposed stabilization techniques include path-length regularization [37], expressive latent priors [38], and adaptive-step solvers with adjoint methods [15]. These have not been evaluated for coupled multi-body ODE estimation from video; the catastrophic divergence exposed by IRIS (Sec. 6.3) suggests that such mechanisms may be essential for extending latent-space parameter estimation to interacting systems.

3 The IRIS Benchmark

3.1 Task Definition

IRIS targets *physics identification from monocular video*: given frames $\mathcal{V} = \{I_1, \dots, I_T\}$, the objectives are to (i) identify the governing dynamical system from a bank of K candidate ODEs $\{\mathcal{P}_1, \dots, \mathcal{P}_K\}$ and (ii) estimate its physical parameters γ without supervision or metadata. The observed motion is assumed driven by a low-dimensional latent state $\mathbf{z}_t \in \mathbb{R}^d$ evolving according to an ODE. For multi-body systems, the state extends to $\mathbf{Z}_t \in \mathbb{R}^{N \times d}$.

3.2 Design Principles

IRIS is constructed around four principles: (1) **controlled recording** under fixed lighting and stable camera placement; (2) **high resolution and frame rate** at 4K/60 fps; (3) **independent ground truth** measured with calibrated instruments with uncertainty estimates; (4) **repeated trials** with 10 recordings per setting, enabling variance analysis.

3.3 Why Real Data?

Synthetic benchmarks provide exact ground truth and reproducibility but suffer from a domain gap that is particularly acute for inverse problems: rendering engines employ idealized geometry, lighting, and contact models, and estimators

Table 1: **Phenomenon–ODE mapping.** *Physical ODE*: governing equation in SI units. *ODE bank form*: parameterization used in the candidate library. *Target params*: parameters estimated from video.

Phenomenon	Physical ODE	ODE bank form	Target params	Notes
<i>Single-body</i>				
Dropping ball	$z'' = -g$	$z'' + \beta z' + \alpha z = 0$	$\alpha \approx g, \beta$	Local linearization
Falling ball	$r(t) = r_0 f / (h_0 + \frac{1}{2} g t^2)$	1 st -order apparent-size	g, r_0, f, h_0	Exact geometric proj.
Sliding cone	$x'' = g(\sin \alpha - \mu \cos \alpha)$	Constant accel. $x'' = a$	α [deg], μ	Exact; a via known g
Pendulum	$\theta'' + \zeta \theta' + (g/L) \sin \theta = 0$	Same (nonlinear $\sin \theta$)	L [m], ζ, g	Exact; no small-angle
Rotating cone	$\varphi'' + \beta \varphi' + \alpha \varphi = 0$	Same (damped torsional)	α, β	Exact
<i>Multi-body</i>				
Hitting cones	Multi-body contact	$z_i'' + \zeta z_i' + \kappa \sum_j (z_i - z_j) = 0$	κ, ζ	Simplified; see text
Two mov. pend.	Eq. 1	Same (coupled $\sin \theta$)	$L_i, \zeta_i, \kappa_{ij}$	Simplified; see text
One stat. pend.	Eq. 1	Same (coupled $\sin \theta$)	$L_i, \zeta_i, \kappa_{ij}$	Simplified; see text

calibrated on synthetic data may fail to transfer to the motion blur, partial occlusions, and material variability present in real video [7]. IRIS provides a real-world testbed with independently measured ground truth while maintaining controlled experimental conditions and repeatability. The domain gap between synthetic and real data is especially relevant for multi-body scenarios, where contact dynamics produce complex visual phenomena (deformation, occlusion, scattering) that are difficult to simulate faithfully.

3.4 Physical Phenomena and ODE Bank

IRIS covers both **single-body** and **multi-body** phenomena. Table 1 provides the explicit mapping between each phenomenon, its physical ODE, the ODE bank form used for estimation, and the target parameters. For the *dropping ball*, the physical dynamics are governed by $z'' = -g$; however, the ODE bank employs a unified second-order linear form $z'' + \beta z' + \alpha z = 0$ following prior work [2, 3], where α absorbs the gravitational constant in latent units and requires calibration to yield physical g . For multi-body phenomena, contact is modeled via a coupling coefficient κ_{ij} that is continuously active, rather than through explicit impact mechanics; this simplification is discussed further below.

Single-body dynamics comprises five phenomena, each recorded under multiple experimental settings:

1. *Dropping ball*: a ball released from rest at height h_0 [m], undergoing free fall. Three drop heights are recorded: 50 cm, 100 cm, and 150 cm.
2. *Falling ball*: a ball filmed during free fall from above, with apparent radius governed by $r(t) = r_0 f / (h_0 + \frac{1}{2} g t^2)$. Three balls of different physical size are used (big: $r_0 = 0.11$ m; mid: $r_0 = 0.07$ m; small: $r_0 = 0.04$ m).
3. *Sliding cone*: a cone sliding down an inclined plane, governed by $x''(t) = g(\sin \alpha - \mu \cos \alpha)$. Three inclination angles are recorded: 45° , 60° , and 80° .

4. *Pendulum*: a damped pendulum described by $\theta''(t) + \zeta\theta'(t) + (g/L)\sin\theta(t) = 0$. Three initial release angles are recorded: 20° , 45° , and 90° , with larger amplitudes probing the nonlinear $\sin\theta$ regime (Appendix J).
5. *Rotating cone*: a cone on a rotating wooden support, modeled as a damped torsional oscillator $\varphi''(t) + \beta\varphi'(t) + \alpha\varphi(t) = 0$. Three rotational speeds are defined by initial displacement: *slow* (half-circle), *mid* (one full circle), and *fast* (two full circles).

Multi-body dynamics introduces three novel interaction scenarios. *Important modeling caveat*: contact between bodies is modeled via a continuously active coupling coefficient κ_{ij} rather than through physically rigorous impact mechanics. This deliberate simplification ensures compatibility with existing latent-space estimation pipelines [2, 3, 7], which require smooth, differentiable dynamics. The recovered κ_{ij} represents effective interaction strength rather than a physically grounded contact coefficient.

1. *Hitting cones*: a ball launched toward a 5-4-3-2-1 pyramid of 15 cones (bottom two rows blue, top three rows red), testing recovery of contact-force and damping parameters from multi-object collision dynamics.
2. *Two moving pendulums*: two pendulums released simultaneously from the same initial angle θ_0 , colliding at the bottom. Three initial angles (20° , 45° , 90°) vary the collision energy. The coupled system is governed by

$$\theta_i''(t) + \zeta_i\theta_i'(t) + \frac{g}{L_i}\sin\theta_i(t) + \kappa_{ij}(\theta_i(t) - \theta_j(t)) = 0, \quad i \neq j, \quad (1)$$

where L_i [m] is rope length, ζ_i [s⁻¹] is damping, and κ_{ij} [s⁻²] is the coupling coefficient.

3. *One static, one moving pendulum*: one pendulum hangs at rest while a second is released from the left, strikes the stationary pendulum, and both come to rest through repeated collisions. Three release angles (20° , 45° , 90°) test sensitivity to initial energy and interaction asymmetry.

Each single-body phenomenon contains 3 settings; multi-body phenomena contain 1–3 settings, yielding 22 settings and 220 videos in total. Figure 1 presents representative frames. Table 2 summarizes the dataset.

3.5 Annotations and Ground Truth

For each recording IRIS provides: (1) video clips in tensor format (N, n_f, C, H, W) ; (2) ground-truth physical parameters with uncertainty bounds in `parameters.json`; (3) equation family labels. Per-frame segmentation masks via SAM2 [39] are provided for multi-object setups. A calibration checkerboard enables metric-scale recovery.

Ground-truth measurement of damping and friction. Damping and friction coefficients carry larger uncertainty than geometric quantities. For the *pendulum damping coefficient* ζ , ground truth is obtained by fitting an exponential decay

Table 2: **IRIS dataset summary.** Each setting contains 10 repeated recordings across diverse physical phenomena.

Type	Phenomenon	# Set.	# Vid.	Dur. (s)	GT Params
<i>Single</i>	Dropping ball	3	30	5	g, β
	Falling ball	3	30	8	g, r_0, f, h_0
	Sliding cone	3	30	5	μ, α
	Pendulum	3	30	150	L, ζ, g
	Rotating cone	3	30	8	α, β
<i>Multi</i>	Hitting cones	1	10	5	κ, ζ
	Two moving pend.	3	30	6	$L_i, \zeta_i, \kappa_{ij}$
	One static pend.	3	30	20	$L_i, \zeta_i, \kappa_{ij}$
Total		22	220	–	–

envelope $A(t) = A_0 e^{-\zeta t/2}$ to peak amplitudes from extended-duration recordings (~ 150 s per clip), with uncertainty quantified as the 95% confidence interval across the 10 trials per setting. For the *friction coefficient* μ , ground truth is obtained from $\mu = \tan \alpha - a_{\text{measured}}/(g \cos \alpha)$, with uncertainty propagated from the standard deviation of a_{measured} across trials. For the *torsional damping* β , the same exponential-envelope fitting is applied. Damping ground truth is derived from trajectory fits rather than independent physical measurement; this distinction is documented in `parameters.json` via a `measurement_type` field ("direct" vs. "fitted").

Train/val/test splits. For each (phenomenon, setting), the 10 repeated recordings are split 7/1/2 (train/val/test). Because the pipeline trains per clip (no cross-clip parameter sharing), the split affects only aggregation statistics: MAE and $\sigma_{\hat{\theta}}$ in result tables are computed over the 2 test clips per setting unless stated otherwise. Split assignments are fixed and released with the dataset to ensure reproducibility. A held-out leaderboard partition is reserved for future community evaluation.

3.6 Comparison with Existing Benchmarks

Table 3 compares IRIS with existing benchmarks. IRIS is the first real-world benchmark combining multi-body interaction dynamics with ground-truth physical parameters, while providing substantially higher resolution and more repeated trials per setting than prior datasets.

4 Evaluation Protocol

A central contribution of IRIS is a method-agnostic evaluation protocol enabling fair comparison.

Table 3: **Comparison with existing benchmarks** for physical parameter estimation from video.

Benchmark	Real	Resolution	Videos	Phen.	Multi	GT	Trials
PAIG synth. [3]	✗	50×50	var.	1	✗	✗	–
NIRPI synth. [2]	✗	100×100	var.	2	✗	✗	–
Physics101 [20]	✓	1280×720	101	17	✗	✗	1
VideoPhy [21]	✓	var.	688	–	✗	✗	–
Delfys75 [7]	✓	1920×1080	75	5	✗	✓	5
IRIS (ours)	✓	3840×2160	220	8	✓	✓	10

Train-per-clip protocol. For every video clip, independently: (i) the equation family is determined; (ii) the physics model is instantiated; (iii) the model is trained on that clip from scratch. No parameters are shared across clips. The random seed is fixed for reproducibility.

Evaluation axes. Five axes are defined. *Parameter accuracy* (primary) measures closeness to ground truth via MAE: $\text{MAE} = n^{-1} \sum_{i=1}^n |\hat{\theta}_i - \theta^*|$, with estimation standard deviation $\sigma_{\hat{\theta}}$ for stability. *Equation selection accuracy* measures correct ODE assignment via overall and per-class accuracy with confusion matrices. *Identifiability* is assessed through gradient norms $G_{\hat{\gamma}}^{(e)} = \|\nabla_{\hat{\gamma}} \mathcal{L}^{(e)}\|_2$ at epoch e and the ODE residual $\mathcal{R} = (T-1)^{-1} \sum_t \|\hat{\mathbf{z}}_{t+1} - \mathcal{P}(\hat{\mathbf{z}}_t; \hat{\gamma}, \Delta t)\|^2$. *Robustness* measures consistency across design choices. *Extrapolation* evaluates prediction beyond the training horizon via:

$$\mathcal{E}_k = \|\hat{\mathbf{z}}_k - \tilde{\mathbf{z}}_k\|^2, \quad k > T_{\text{train}}, \quad (2)$$

where $\hat{\mathbf{z}}_k$ is obtained by unrolling the learned ODE from the last training frame and $\tilde{\mathbf{z}}_k$ is the encoder output for the held-out frame I_k .

Data and reproducibility. All reported numbers are produced by a single evaluation script operating on fixed CSV outputs. Each table entry is traceable to a specific (phenomenon, setting, clip, seed) tuple. MAE values are computed over the test partition (2 clips per setting) unless stated otherwise. The evaluation code, CSV outputs, and random seeds are released with the dataset.

5 Baselines

Representative baselines are evaluated to establish reference performance and expose failure modes. All follow the train-per-clip protocol with identical ground-truth sources.

5.1 Latent-Space Baseline

The primary baseline is the latent-space pipeline of Garcia et al. [7]: an encoder maps frames to latent states, a physics block implements a discrete-time ODE

step, and training minimizes $\mathcal{L}_{1\text{-step}} = M^{-1} \sum_i \|\hat{\mathbf{z}}_i - \tilde{\mathbf{z}}_i\|^2 + \mathcal{L}_{\text{KL}}$, with path-based equation selection.

Gradient-flow diagnosis. Baseline evaluation on IRIS revealed a critical bug in the original Euler integrator: the position update omits the acceleration term, severing gradient flow to γ . A *corrected* variant restores the standard update $z_{t+1} = z_t + \Delta t z_t^{(1)} + \Delta t^2 z_t^{(2)}$.

5.2 Multi-Step Loss Variant

The corrected baseline is evaluated with a multi-step rollout loss enforcing agreement over K future horizons:

$$\mathcal{L}_{\text{total}} = \sum_{k=1}^K w_k \|\hat{\mathbf{z}}_{t+k} - \tilde{\mathbf{z}}_{t+k}\|^2 + \mathcal{L}_{\text{KL}}(\hat{\mathbf{z}}), \quad (3)$$

where $\tilde{\mathbf{z}}_{t+k}$ is obtained by unrolling k physics steps from $\hat{\mathbf{z}}_t$ and w_k decays geometrically ($w = [1, 1, 0.5, 0.5, 0.25]$ for $K=5$). The rationale is that one-step supervision can underconstrain γ : multi-step rollouts accumulate the effect of physical parameters over time, providing a denser gradient signal.

5.3 Equation-Identification Strategies

IRIS benchmarks four complementary strategies for governing-equation identification:

(1) VLM temporal reasoning. A VLM acts as a routing function $k^* = \text{VLM}(\{I_{s_1}, \dots, I_{s_m}\}; \mathcal{C}_1, \dots, \mathcal{C}_K)$, where $m=5$ frames are sampled at $t = 0\%, 25\%, 50\%, 75\%, 100\%$ and \mathcal{C}_k is a natural-language class description. Three VLM backends are evaluated: GPT-4V, LLaVA-Video-7B, and InternVL2-8B.

(2) Describe-then-classify. A two-stage VLM pipeline: the first call generates a free-form description of the observed motion; the second classifies the description into one of the K equation families. This decouples visual perception from physical classification.

(3) CNN video classifier. A lightweight ResNet-18 with temporal mean pooling, trained on the same distribution as the evaluation data, representing the upper bound of in-distribution performance. The CNN requires retraining whenever the phenomenon set changes, whereas VLM strategies operate zero-shot.

(4) Path-based labels (oracle). Ground-truth equation family provided by folder structure, serving as the oracle condition.

ODE bank. The library comprises: second-order linear (damped oscillator), first-order exponential decay, first-order nonlinear (Torricelli), constant acceleration (sliding), and coupled oscillator (Eq. 1).

Latent-to-SI calibration. Because latent-space baselines map frames to an arbitrary latent space, a per-phenomenon canonical normalization converts latent ODE coefficients to SI units: pendulum L via period extraction ($L = g(T/2\pi)^2$), free-fall g via spatial scale factor from known object dimensions, friction μ from

dimensionless acceleration ratios. These calibration heuristics are phenomenon-specific and depend on the encoder’s latent geometry, which may introduce systematic bias. IRIS provides calibration infrastructure (checkerboard frames, known object dimensions) but does not eliminate the underlying ambiguity. Full details are in Appendix D.

6 Experiments

Baselines are evaluated along five axes: parameter estimation accuracy (primary), governing-equation identification, identifiability, extrapolation, and component ablations. All experiments follow the train-per-clip protocol with a fixed random seed (42) and shared CSV output format.

6.1 Experimental Setup

Three configurations are compared: (1) **Baseline**: path-based equation selection, one-step loss, original uncorrected Euler integrator [7]; (2) **+Corrected**: gradient-corrected Euler step, one-step loss; (3) **+Multi-step**: corrected integrator with multi-step rollout loss ($K=5$). Additionally, four equation-identification strategies are evaluated independently.

6.2 Physical Parameter Estimation on Delfys75

Effect of Gradient Correction. Table 4 reports MAE for the original and corrected baselines on Delfys75 [7]. The most prominent result concerns the pendulum: the original baseline yields MAE of 95.07 m on `pendulum_45` for string length, compared to 3.80 m for the corrected variant ($\Delta\text{MAE} = -91.27$ m), a direct consequence of the severed gradient flow. Both variants report MAE ≈ 0 for g on `dropped_ball/large` and `free_fall/mousepad` because the uncorrected integrator leaves g at its initialization value $g_0 = 9.81$, which coincides with ground truth (see Table 4 footnote). Substantial improvements are also observed on Torricelli drainage ($-3.16, -1.99$) and LED 2 s decay (-1.90).

Effect of Multi-Step Loss on Delfys75. Table 5 compares one-step and multi-step losses. Multi-step consistently reduces MAE for g across free fall and dropped ball (largest: $\Delta\text{MAE} = -0.90$ on `free_fall/table`). The `led_10s` setting degrades ($+5.37$) because slow dynamics cause rollout divergence.

6.3 Physical Parameter Estimation on IRIS

Single-body phenomena. On *sliding cone*, both configurations recover the inclination angle exactly (MAE = 0.00). On *rotation*, multi-step loss yields improvements for angular stiffness across all settings ($\Delta\text{MAE} = -0.64, -1.21, -2.11$) but angular damping in the fast setting degrades ($+0.39$). On *pendulum*,

Table 4: **Parameter MAE on Delfys75**: original baseline (uncorrected Euler) vs. corrected variant. **Bold** = lower MAE.

Dynamics	Setting	Param	GT	Base.	Corr.	Δ
Dropped ball	large	g [m/s ²]	9.81	0.00 [†]	0.00	0.00
Free fall	mousepad	g [m/s ²]	9.81	0.00 [†]	0.00	0.00
LED	led_2s	γ	2.30	2.30	0.40	-1.90
Pendulum	pend._45	L [m]	0.45	95.07	3.80	-91.27
	pend._90	L [m]	0.90	50.15	2.93	-47.22
	pend._150	L [m]	1.50	29.83	0.71	-29.12
Sliding bl.	mid	μ	0.21	0.00	0.00	0.00
Torricelli	large	k	0.016	6.07	2.91	-3.16
	small	k	0.010	7.67	5.69	-1.99

[†]Both yield MAE ≈ 0 because $g_0=9.81$ coincides with GT; uncorrected integrator prevents learning.

Table 5: **Multi-step loss vs. one-step on Delfys75** (representative subset; ties omitted). **Bold** = lower MAE.

Dynamics	Setting	Param	1-step	Multi	Δ
Dropped ball	large	g [m/s ²]	0.25	0.18	-0.07
	mousepad	g [m/s ²]	2.12	1.65	-0.47
Free fall	table	g [m/s ²]	1.06	0.15	-0.90
	tennis	g [m/s ²]	1.06	0.53	-0.53
LED	led_10s	γ	2.09	7.46	+5.37
Pendulum	pend._45	L [m]	0.35	0.50	+0.15
Torricelli	large	k	6.27	6.54	+0.27

multi-step improves rope length at 20° (-0.44) but produces catastrophic divergence at 90° (+20.49). On *dropping ball* and *falling ball*, multi-step consistently increases MAE for g .

Multi-body phenomena. The multi-step loss exhibits catastrophic failure on all multi-body scenarios. On *two moving pendulums*, rope length MAE exceeds 100 m across all settings (worst: 741.1 m at 20°), compared to 1.1–3.0 m for the one-step baseline. Errors in the coupling terms κ_{ij} compound exponentially across the $K=5$ horizon, driving parameters far from ground truth. Whether richer impact models or latent ODE stabilization techniques (Sec. 2.6) would mitigate this instability remains an open question. Full per-setting results are reported in Appendix G.

6.4 Identifiability Analysis

Table 6 reports gradient norms $G_\gamma^{(e)}$ at selected epochs and the converged ODE residual \mathcal{R} for representative phenomena under the corrected one-step baseline. Several patterns emerge. The corrected integrator produces non-zero gradient norms at epoch 1 for all phenomena, confirming restored parameter identifiability. Gradient norms decay monotonically for single-body phenomena; the sliding cone converges fastest ($G_\gamma^{(200)} \sim 10^{-6}$), consistent with its exact identifiability. Multi-body phenomena retain substantially larger gradient norms at epoch 200

Table 6: **Identifiability diagnostics:** physics-parameter gradient norms $G_\gamma^{(e)} = \|\nabla_\gamma \mathcal{L}^{(e)}\|_2$ at epochs 1, 50, and 200, and converged ODE residual \mathcal{R} (mean over test clips). The uncorrected baseline yields $G_\gamma \approx 0$ at all epochs (omitted).

Phenomenon	Setting	$G_\gamma^{(1)}$	$G_\gamma^{(50)}$	$G_\gamma^{(200)}$	$\mathcal{R} (\times 10^{-3})$
<i>Single-body</i>					
Pendulum	pend._45	2.4×10^{-2}	8.1×10^{-3}	1.2×10^{-4}	0.83
Rotation	mid	1.8×10^{-2}	5.3×10^{-3}	9.7×10^{-5}	0.41
Sliding cone	cone_60	3.1×10^{-2}	1.4×10^{-4}	2.0×10^{-6}	0.02
Dropping ball	drop_100	1.5×10^{-2}	4.7×10^{-3}	3.8×10^{-4}	1.92
<i>Multi-body</i>					
Two mov. pend.	pend._45	3.8×10^{-2}	2.1×10^{-2}	7.4×10^{-3}	12.6
One stat. pend.	pend._45	4.2×10^{-2}	1.9×10^{-2}	5.1×10^{-3}	9.83

Table 7: **Extrapolation error** \mathcal{E}_k (mean \pm std over test clips) at selected horizons k beyond the training window.

Setting	$\mathcal{E}_{k=10}$	$\mathcal{E}_{k=25}$	$\mathcal{E}_{k=50}$
pend._20	0.008 ± 0.003	0.041 ± 0.012	0.189 ± 0.067
pend._45	0.012 ± 0.005	0.078 ± 0.031	0.402 ± 0.148
pend._90	0.031 ± 0.014	0.217 ± 0.095	1.284 ± 0.531

($\sim 10^{-3}$) and ODE residuals an order of magnitude higher than single-body systems, indicating that the physics block does not fully explain the encoded trajectory, consistent with the simplified contact model (Sec. 3.4).

6.5 Extrapolation Beyond Training Horizon

The extrapolation error \mathcal{E}_k (Eq. 2) is computed for the corrected one-step baseline on the pendulum (150 s clips, trained on the first 100 frames ≈ 1.67 s, extrapolated for 50 additional frames). Extrapolation error grows with both horizon length and initial amplitude: the 90° setting exhibits $\mathcal{E}_{k=50}$ approximately $7\times$ larger than 20° , reflecting compounding nonlinear dynamics. This motivates future work on physics-constrained extrapolation losses and adaptive training horizons.

6.6 Governing Equation Identification

Setup. Three routing strategies are evaluated on both Delfys75 (90 videos, 6 phenomena) and IRIS (240 videos, 8 phenomena). The CNN classifier is trained separately on each benchmark.

Table 8: Equation-selection accuracy by method and dataset. Bold = best per column.

Method	Delfys75 (90)	IRIS (240)
CNN (video classifier)	98.40	99.30
VLM (temporal reasoning)	73.33	65.00
VLM (describe-then-classify)	61.11	72.92

Accuracy. Table 8 reports equation-selection accuracy. On Delfys75, the CNN achieves 98.40%, followed by VLM temporal reasoning (73.33%) and describe-then-classify (61.11%). On IRIS, the CNN achieves 99.30%, but the ranking of VLM strategies reverses: describe-then-classify (72.92%) outperforms temporal reasoning (65.00%). This reversal is attributable to the greater visual diversity of IRIS: the two-stage pipeline allows the VLM to first articulate dynamics in natural language, producing richer intermediate representations that facilitate disambiguation between single- and multi-body phenomena.

Error analysis. The confusion matrix (Appendix E.5) reveals that VLM temporal reasoning errors on Delfys75 are concentrated between physically adjacent classes: dropped ball confused with free fall (5/15), and free fall misclassified as pendulum (10/15). LED, sliding block, and Torricelli are classified without error. On IRIS, multi-body phenomena are classified with higher per-class accuracy due to their distinctive visual signatures.

6.7 Ablation Studies

Gradient correction is the single most impactful component: without it, $G_\gamma^{(e)} \approx 0$ throughout training and all subsequent improvements are negligible.

Multi-step horizon. Ablating $K \in \{1, 2, 3, 5\}$: $K=5$ provides the best trade-off for gravity-dominated phenomena on Delfys75 but produces catastrophic divergence on IRIS multi-body scenarios at all $K > 1$, motivating the application of latent ODE stabilization techniques [37]. Full horizon ablation results are in Appendix K.

VLM prompt strategy. Single-frame prompting achieves 54%, three-frame 67%, and five-frame 73% on Delfys75, confirming temporal context is essential.

Symplectic integrator. Störmer-Verlet achieves lower ODE residual on conservative systems with comparable performance on non-conservative phenomena. Full comparison in Appendix L.

7 Open Challenges Exposed by IRIS

The baseline evaluation reveals systematic failure modes that define open challenges.

Equation identification remains a bottleneck. VLM routing achieves 65–73% on IRIS depending on prompt strategy, with misclassification propagating directly into parameter error. No single prompting approach generalizes reliably across benchmarks; CNN classifiers achieve near-perfect accuracy but require per-distribution retraining.

Multi-step training fails on multi-body dynamics. Multi-step loss improves identifiability on selected single-body phenomena but produces errors exceeding 10^2 m on multi-body scenarios, where coupling terms κ_{ij} amplify integration error exponentially. Addressing this may require truncated rollouts, adaptive horizon scheduling, or contact-aware integration [37, 38].

Damping is poorly identifiable. Damping coefficients exhibit substantially higher relative error than conservative parameters across all baselines, requiring longer observation windows or specialized loss terms.

Latent-to-SI calibration introduces bias. Converting latent coefficients to SI units requires per-phenomenon normalization dependent on encoder geometry; cross-phenomenon MAE comparisons should be interpreted accordingly.

8 Limitations and Future Work

Dataset scope. IRIS is of moderate scale with a fixed set of phenomena. Ground truth for damping is derived from trajectory fits rather than independent physical measurement (Sec. 3.5). Dense segmentation masks are not yet available for every multi-body clip.

Contact model simplification. Multi-body interactions use a continuously active coupling coefficient rather than rigorous impact mechanics. Extending the ODE bank to incorporate richer contact models [33, 34] is an important future direction.

Baseline coverage. Hamiltonian/Lagrangian approaches [16, 17], SINDy [1], graph neural simulators [18], and differentiable contact pipelines [33] are not yet evaluated. Latent ODE stabilization techniques [37, 38] may mitigate multi-step instability but have not been tested. The protocol accommodates these without modification.

Planned extensions. Additional phenomena (rolling, bouncing, fluid-like motion); larger scale with multi-view data; richer annotations; cross-dataset evaluation with physics-plausibility benchmarks [23–25]; downstream task metrics.

9 Conclusion

This work introduces IRIS, a high-fidelity real-world benchmark for physics identification from monocular video comprising 220 videos at 4K resolution spanning eight dynamical systems, including three novel multi-body scenarios, with ground-truth parameters and uncertainty estimates. A standardized five-axis evaluation protocol enables fair comparison. Four equation-identification strategies are benchmarked, revealing that VLM strategy rankings reverse across

benchmarks while CNN classifiers achieve near-perfect in-distribution accuracy. A multi-step loss variant improves identifiability on selected single-body dynamics but exposes catastrophic instabilities on multi-body scenarios. These findings, together with the diagnosis of a gradient-flow bug in the state-of-the-art pipeline, demonstrate the diagnostic value of rigorous benchmarking and define concrete open problems.

Acknowledgements

Omitted for anonymized submission.

References

- [1] Steven L. Brunton, Joshua L. Proctor, and J. Nathan Kutz. “Discovering governing equations from data by sparse identification of nonlinear dynamical systems”. In: *Proceedings of the National Academy of Sciences* 113.15 (2016), pp. 3932–3937.
- [2] Florian Hofherr, Lukas Koestler, Florian Bernard, and Daniel Cremers. “Neural implicit representations for physical parameter inference from a single video”. In: *Proceedings of the IEEE/CVF Winter Conference on Applications of Computer Vision (WACV)*. 2023, pp. 2093–2103.
- [3] Miguel Jaques, Michael Burke, and Timothy Hospedales. “Physics-as-inverse-graphics: Unsupervised physical parameter estimation from video”. In: *arXiv preprint arXiv:1905.11169* (2019).
- [4] Michael Schmidt and Hod Lipson. “Distilling free-form natural laws from experimental data”. In: *Science* 324.5923 (2009), pp. 81–85.
- [5] Filipe de Avila Belbute-Peres, Kevin Smith, Kelsey Allen, Josh Tenenbaum, and J. Zico Kolter. “End-to-end differentiable physics for learning and control”. In: *Advances in Neural Information Processing Systems (NeurIPS)* 31 (2018).
- [6] Petar Veličković, Matko Bošnjak, Thomas Kipf, et al. “Reasoning-modulated representations”. In: *Learning on Graphs Conference*. PMLR. 2022, pp. 50–1.
- [7] Alejandro Castañeda Garcia, Jan Warchocki, Jan van Gemert, Daan Brinks, and Nergis Tomen. “Learning physics from video: Unsupervised physical parameter estimation for continuous dynamical systems”. In: *Proceedings of the IEEE/CVF Conference on Computer Vision and Pattern Recognition (CVPR)*. 2025, pp. 27924–27933.
- [8] Martin Asenov, Michael Burke, Daniel Angelov, Todor Davchev, Kartic Subr, and Subramanian Ramamoorthy. “Vid2Param: Modeling of dynamics parameters from video”. In: *IEEE Robotics and Automation Letters* 5.2 (2019), pp. 414–421.
- [9] Nicholas Watters, Daniel Zoran, Theophane Weber, Peter Battaglia, Razvan Pascanu, and Andrea Tacchetti. “Visual interaction networks: Learning a physics simulator from video”. In: *Advances in Neural Information Processing Systems (NeurIPS)* 30 (2017).
- [10] Jiajun Wu, Ilker Yildirim, Joseph J. Lim, Bill Freeman, and Josh Tenenbaum. “Galileo: Perceiving physical object properties by integrating a physics engine with deep learning”. In: *Advances in Neural Information Processing Systems (NeurIPS)* 28 (2015).

- [11] Jiajun Wu, Erika Lu, Pushmeet Kohli, Bill Freeman, and Josh Tenenbaum. “Learning to see physics via visual de-animation”. In: *Advances in Neural Information Processing Systems (NeurIPS)* 30 (2017).
- [12] Tsung-Yen Yang, Justinian Rosca, Karthik Narasimhan, and Peter J. Ramadge. “Learning physics constrained dynamics using autoencoders”. In: *Advances in Neural Information Processing Systems (NeurIPS)* 35 (2022), pp. 17157–17172.
- [13] David Zheng, Vinson Luo, Jiajun Wu, and Joshua B. Tenenbaum. “Unsupervised learning of latent physical properties using perception-prediction networks”. In: *arXiv preprint arXiv:1807.09244* (2018).
- [14] Peter Toth, Danilo Jimenez Rezende, Andrew Jaegle, Sébastien Racanière, Aleksandar Botev, and Irina Higgins. “Hamiltonian generative networks”. In: *arXiv preprint arXiv:1909.13789* (2019).
- [15] Ricky T. Q. Chen, Yulia Rubanova, Jesse Bettencourt, and David K. Duvenaud. “Neural ordinary differential equations”. In: *Advances in Neural Information Processing Systems (NeurIPS)*. Vol. 31. 2018, pp. 6571–6583.
- [16] Samuel Greycanus, Misko Dzamba, and Jason Yosinski. “Hamiltonian neural networks”. In: *Advances in Neural Information Processing Systems (NeurIPS)*. Vol. 32. 2019, pp. 15353–15363.
- [17] Miles Cranmer, Sam Greycanus, Stephan Hoyer, Peter Battaglia, David Spergel, and Shirley Ho. “Lagrangian neural networks”. In: *ICLR Workshop on Integration of Deep Neural Models and Differential Equations*. 2020.
- [18] Alvaro Sanchez-Gonzalez, Jonathan Godwin, Tobias Pfaff, Rex Ying, Jure Leskovec, and Peter W. Battaglia. “Learning to simulate complex physics with graph networks”. In: *Proceedings of the International Conference on Machine Learning (ICML)*. Vol. 119. PMLR. 2020, pp. 8459–8468.
- [19] Peter W. Battaglia, Razvan Pascanu, Matthew Lai, Danilo Rezende, and Koray Kavukcuoglu. “Interaction networks for learning about objects, relations and physics”. In: *Advances in Neural Information Processing Systems (NeurIPS)*. Vol. 29. 2016, pp. 4502–4510.
- [20] Jiajun Wu, Joseph J. Lim, Hongyi Zhang, Joshua B. Tenenbaum, and William T. Freeman. “Physics 101: Learning physical object properties from unlabeled videos”. In: *British Machine Vision Conference (BMVC)*. 2016.
- [21] Hritik Bansal, Zongyu Lin, Tianyi Xie, et al. “VideoPhy: Evaluating physical commonsense for video generation”. In: *arXiv preprint arXiv:2406.03520* (2024).
- [22] Saman Motamed, Laura Culp, Kevin Swersky, Priyank Jaini, and Robert Geirhos. “Do generative video models understand physical principles?” In: *Proceedings of the IEEE/CVF Winter Conference on Applications of Computer Vision (WACV)*. 2026, pp. 948–958.
- [23] Chenyu Zhang, Daniil Cherniavskii, Antonios Tragoudaras, et al. *Morpheus: Benchmarking Physical Reasoning of Video Generative Models with Real Physical Experiments*. 2025. arXiv: 2504.02918 [cs.CV]. URL: <https://arxiv.org/abs/2504.02918>.
- [24] Meng-Hao Guo, Jiajun Xu, Yi Zhang, et al. *R-Bench: Graduate-level Multi-disciplinary Benchmarks for LLM & MLLM Complex Reasoning Evaluation*. 2025. arXiv: 2505.02018 [cs.CV]. URL: <https://arxiv.org/abs/2505.02018>.
- [25] Ao Liang, Lingdong Kong, Tianyi Yan, et al. *WorldLens: Full-Spectrum Evaluations of Driving World Models in Real World*. 2025. arXiv: 2512.10958 [cs.CV]. URL: <https://arxiv.org/abs/2512.10958>.

- [26] Konstantinos I. Roumeliotis and Nikolaos D. Tselikas. “ChatGPT and open-AI models: A preliminary review”. In: *Future Internet* 15.6 (2023), p. 192.
- [27] Haotian Liu, Chunyuan Li, Qingyang Wu, and Yong Jae Lee. “Visual instruction tuning”. In: *Advances in Neural Information Processing Systems (NeurIPS)* 36 (2023), pp. 34892–34916.
- [28] Yuanhan Zhang, Jinming Wu, Wei Li, et al. “LLaVA-Video: Video instruction tuning with synthetic data”. In: *arXiv preprint arXiv:2410.02713* (2024).
- [29] Vahid Balazadeh, Mohammadmehdi Ataei, Hyunmin Cheong, Amir Hosein Khasahmadi, and Rahul G. Krishnan. “Physics context builders: A modular framework for physical reasoning in vision-language models”. In: *Proceedings of the IEEE/CVF International Conference on Computer Vision (ICCV)*. 2025, pp. 7318–7328.
- [30] Jiaqi Liu, Songning Lai, Pengze Li, et al. “Mimicking the Physicist’s Eye: A VLM-centric Approach for Physics Formula Discovery”. In: *arXiv preprint arXiv:2508.17380* (2025).
- [31] Kathleen Champion, Bethany Lusch, J. Nathan Kutz, and Steven L. Brunton. “Data-driven discovery of coordinates and governing equations”. In: *Proceedings of the National Academy of Sciences* 116.45 (2019), pp. 22445–22451.
- [32] Ruikun Li, Yan Lu, Shixiang Tang, Biqing Qi, and Wanli Ouyang. *MLLM-based Discovery of Intrinsic Coordinates and Governing Equations from High-Dimensional Data*. 2025. arXiv: 2505.11940 [cs.CE].
- [33] Meizhong Wang, Wanxin Jin, Kun Cao, Lihua Xie, and Yiguang Hong. *ContactGaussian-WM: Learning Physics-Grounded World Model from Videos*. 2026. arXiv: 2602.11021 [cs.R0]. URL: <https://arxiv.org/abs/2602.11021>.
- [34] Yiren Song, Xiaokang Liu, and Mike Zheng Shou. *DiffSim: Taming Diffusion Models for Evaluating Visual Similarity*. 2024. arXiv: 2412.14580 [cs.CV]. URL: <https://arxiv.org/abs/2412.14580>.
- [35] Jonas Degraeve, Michiel Hermans, Joni Dambre, and Francis wyffels. *A Differentiable Physics Engine for Deep Learning in Robotics*. 2018. arXiv: 1611.01652 [cs.NE]. URL: <https://arxiv.org/abs/1611.01652>.
- [36] Keenon Werling, Dalton Omens, Jeongseok Lee, Ioannis Exarchos, and C. Karen Liu. *Fast and Feature-Complete Differentiable Physics for Articulated Rigid Bodies with Contact*. 2021. arXiv: 2103.16021 [cs.R0]. URL: <https://arxiv.org/abs/2103.16021>.
- [37] Chris Finlay, Jörn-Henrik Jacobsen, Levon Nurbekyan, and Adam M Oberman. *How to train your neural ODE: the world of Jacobian and kinetic regularization*. 2020. arXiv: 2002.02798 [stat.ML]. URL: <https://arxiv.org/abs/2002.02798>.
- [38] Sifan Wang, Hanwen Wang, and Paris Perdikaris. *Learning the solution operator of parametric partial differential equations with physics-informed DeepOnets*. 2021. arXiv: 2103.10974 [cs.LG]. URL: <https://arxiv.org/abs/2103.10974>.
- [39] Nikhila Ravi, Valentin Gabeur, Yuan-Ting Hu, et al. *SAM 2: Segment Anything in Images and Videos*. 2024. arXiv: 2408.00714 [cs.CV].

Supplementary Material

IRIS: A Real-World Benchmark for Inverse Recovery and Identification of Physical Dynamic Systems from Monocular Video

A Dataset Statistics and Release Details

Table S1 provides a complete per-phenomenon, per-setting breakdown of the IRIS dataset. All ground-truth physical parameters are obtained through direct manual measurement using calibrated instruments (see Appendix C), with the exception of damping and friction coefficients, which are derived from trajectory fits as described in Appendix C. Each parameter entry records mean, standard deviation, minimum, and maximum values; where the standard deviation is zero, the measurement reflects a single precisely controlled experimental condition.

Table S1: **Full IRIS dataset statistics.** Each row is one setting; n is the number of videos. d_{cam} denotes camera-to-object distance. Measurement type: **D** = direct, **F** = fitted.

Phenomenon	Setting	n	Dur. (s)	Res.	GT params (measured)	Type
<i>Single-body</i>						
Dropping ball	drop_50	10	5	3840×2160	$h_0=0.50$ m, $d_{\text{cam}}=1.94$ m	D
	drop_100	10	5	3840×2160	$h_0=1.00$ m, $d_{\text{cam}}=1.94$ m	D
	drop_150	10	5	3840×2160	$h_0=1.50$ m, $d_{\text{cam}}=1.94$ m	D
Falling ball	big	10	8	3840×2160	$g=9.81$ m/s ² , $r_0=0.11$ m	D
	mid	10	8	3840×2160	$g=9.81$ m/s ² , $r_0=0.07$ m	D
	small	10	8	3840×2160	$g=9.81$ m/s ² , $r_0=0.04$ m	D
Sliding cone	cone_45	10	5	3840×2160	$\alpha=45^\circ$, hyp. =0.77 m, μ (fit)	D / μ :F
	cone_60	10	5	3840×2160	$\alpha=60^\circ$, hyp. =0.84 m, μ (fit)	D / μ :F
	cone_80	10	5	3840×2160	$\alpha=80^\circ$, hyp. =0.80 m, μ (fit)	D / μ :F
Pendulum	pend._20	10	150	3840×2160	$\theta_0=20^\circ$, $L=0.50$ m, ζ (fit)	D / ζ :F
	pend._45	10	150	3840×2160	$\theta_0=45^\circ$, $L=0.50$ m, ζ (fit)	D / ζ :F
	pend._90	10	150	3840×2160	$\theta_0=90^\circ$, $L=0.50$ m, ζ (fit)	D / ζ :F
Rotating cone	slow	10	8	3840×2160	Half-circle init., β (fit)	D / β :F
	mid	10	8	3840×2160	1-circle init., β (fit)	D / β :F
	fast	10	8	3840×2160	2-circle init., β (fit)	D / β :F
<i>Multi-body</i>						
Hitting cones	default	10	5	3840×2160	$d_{\text{ball-cones}}=2.00$ m, $d_{\text{cam}}=2.20$ m	D
Two mov. pendulums	pend._20	10	6	3840×2160	$\theta_0=20^\circ$, $L_1=L_2=0.50$ m	D
	pend._45	10	6	3840×2160	$\theta_0=45^\circ$, $L_1=L_2=0.50$ m	D
	pend._90	10	6	3840×2160	$\theta_0=90^\circ$, $L_1=L_2=0.50$ m	D
One stat. pendulum	pend._20	10	20	3840×2160	$\theta_0=20^\circ$, $L_1=L_2=0.50$ m	D
	pend._45	10	20	3840×2160	$\theta_0=45^\circ$, $L_1=L_2=0.50$ m	D
	pend._90	10	20	3840×2160	$\theta_0=90^\circ$, $L_1=L_2=0.50$ m	D
Total		220	–	–	–	–

B Physical Model Derivations and ODE Bank

This appendix makes explicit which physical ODE governs each phenomenon, how the latent-space parameterisation (α, β) relates to physical constants, and where the pipeline’s ODE form differs from the exact physical equation.

B.1 Phenomenon–ODE Correspondence Table

Table S2 summarises the mapping from IRIS/Delfys75 phenomena to physical ODEs and to the latent ODE form used in the pipeline.

Table S2: **Phenomenon–ODE correspondence.** “Physical ODE” is the exact governing equation. “Pipeline ODE form” is the form used by the encoder–physics block. “Latent \rightarrow SI” lists the conversion from fitted (α, β) to physical parameters.

Phenomenon	Physical ODE	Pipeline ODE form	Latent \rightarrow SI	Note
Dropping ball	$\ddot{z} = -g$ (constant accel.)	$\ddot{z} + \beta\dot{z} + \alpha z = 0$	$g = \alpha$	Unified linear form; β absorbs drag
Falling ball	$r(t) = r_0 f / (h_0 + \frac{1}{2} g t^2)$	$\ddot{z} + \beta\dot{z} + \alpha z = 0$	$g = \alpha$	Apparent radius; same latent form
Pendulum (small angle)	$\ddot{\theta} + \zeta\dot{\theta} + (g/L)\theta = 0$	$\ddot{z} + \beta\dot{z} + \alpha z = 0$	$L = g/\alpha, \zeta = -\beta$	Exact match for small angles
Rotating cone	$\ddot{\varphi} + \beta\dot{\varphi} + \alpha\varphi = 0$	$\ddot{z} + \beta\dot{z} + \alpha z = 0$	$\alpha_{SI} = \alpha, \beta_{SI} = \beta$	Exact match
Sliding cone	$\ddot{x} = g(\sin \alpha - \mu \cos \alpha)$	Constant-acceleration block	$\mu = \beta$; angle from metadata	Angle fixed from setting
LED decay	$\dot{z} = -\lambda z$	First-order decay block	$\gamma = \beta$	First-order; α unused
Torricelli drain	$\dot{z} = -k\sqrt{z}$	Torricelli block	$k = \alpha$	Nonlinear; separate block
Hitting cones	Momentum transfer (impact)	Graph ODE, coupling κ_{ij}	κ_{ij} (spring-like)	Simplified; see App. H
Two pendulums	$\ddot{\theta}_i + \zeta_i \dot{\theta}_i + (g/L_i)\theta_i + \kappa_{ij}(\theta_i - \theta_j) = 0$	Graph ODE, same form	$L_i = g/\alpha_i, \kappa_{ij}$ (coupling)	Active only during contact

B.2 Design Choice: Unified Linear ODE Bank

The pipeline uses a unified second-order linear ODE $\ddot{z} + \beta\dot{z} + \alpha z = 0$ as the latent representation for all oscillatory and gravity-driven phenomena. This is a deliberate design choice for comparability.

Dropping ball. The true physical ODE is $\ddot{h} = -g$. The pipeline approximates this by $\ddot{z} + \alpha z = 0$ with $\alpha \approx g$; this holds when the encoder maps pixel position linearly to z and the observation window is short enough for the linear approximation to remain valid.

Falling ball (apparent radius). The ball falls away from the camera; the observable is its apparent radius $r(t) = r_0 f / (h_0 + \frac{1}{2} g t^2)$. The latent z encodes this apparent size; the same second-order form is used, and α is compared to g after linear conversion.

Pendulum. For small oscillation angles ($\theta_0 \leq 45^\circ$), the linearised equation is an exact match to the unified ODE form, with $\alpha = g/L$ and $\beta = \zeta$. For large angles ($\theta_0 = 90^\circ$), the linearisation error is substantial, and the fitted α will deviate from g/L . This is a **known modelling limitation**: on the pend..90 setting, higher parameter error is expected and should be interpreted as an identifiability challenge.

B.3 Dropping Ball vs. Falling Ball: Symbol Definitions

- **Dropping ball:** camera is placed *to the side*. The observable is the *vertical pixel position*. Ground truth: $h_0 \in \{0.50, 1.00, 1.50\}$ m, $d_{\text{cam}} = 1.94$ m.
- **Falling ball:** camera is placed *directly above*. The observable is the *apparent radius*. Ground truth: $r_0 \in \{0.04, 0.07, 0.11\}$ m; $g = 9.81$ m/s².

C Ground-Truth Measurement Protocol

C.1 Directly Measured Parameters

Parameters labelled **D** in Table S1 are obtained through direct measurement before or after recording:

- **Heights and lengths** (h_0, L, L_1, L_2 , hypotenuse): measured with a rigid tape measure to the nearest millimetre. Uncertainty: ± 2 mm for lengths up to 1 m, ± 5 mm for longer spans.
- **Angles** (θ_0, α): set with an adjustable protractor or inclinometer calibrated to $\pm 0.5^\circ$.
- **Distances** ($d_{\text{cam}}, d_{\text{ball-cones}}$): measured with a laser distance meter (accuracy ± 2 mm).
- **Ball radius** (r_0): measured with digital calipers (resolution 0.01 mm).
- **Gravitational acceleration** (g): taken as 9.81 m/s^2 (standard local value).

C.2 Fitted Parameters: Damping and Friction

Parameters labelled **F** are estimated from recorded video trajectories:

Damping coefficients (ζ for pendulum, β for rotating cone). The object’s position is tracked frame by frame; the time series is fitted to the analytical damped oscillator solution using nonlinear least squares (Levenberg-Marquardt). Uncertainty: $\sigma_\zeta < 0.01 \text{ s}^{-1}$ for pendulum, $\sigma_\beta < 0.005 \text{ s}^{-1}$ for rotating cone.

Friction coefficient (μ for sliding cone). Acceleration a is estimated from a second-order polynomial fit to the position time series. Then $\mu = \tan \alpha - a/(g \cos \alpha)$. Typical $\sigma_\mu < 0.02$.

Limitations. Fitted parameters carry tracker and model error. For large oscillation angles ($\theta_0 = 90^\circ$), the small-angle approximation in the linear-ODE fit is less accurate, and the reported ζ should be interpreted as *effective* damping under the linearised model.

D Latent-to-Physical Parameter Calibration

The encoder maps raw pixel intensities to a dimensionless latent z_t . To obtain physical parameters, per-phenomenon conversions are applied:

Table S3: Per-phenomenon calibration and physical parameter extraction.

Phenomenon	Extracted param.	Formula	Assumption / note
Dropping ball	$g \text{ [m/s}^2\text{]}$	$g = \alpha_{\text{fit}}$	Latent = pixel height; dt in seconds
Falling ball	$g \text{ [m/s}^2\text{]}$	$g = \alpha_{\text{fit}}$	Latent = apparent radius
Pendulum	$L \text{ [m]}$	$L = g_{\text{true}}/\alpha_{\text{fit}}$	$g_{\text{true}} = 9.81 \text{ m/s}^2$ fixed
Pendulum	$\zeta \text{ [s}^{-1}\text{]}$	$\zeta = -\beta_{\text{fit}}$	Sign convention
Rotating cone	α, β	direct	Same ODE form
Sliding cone	μ	$\mu = \beta_{\text{fit}}$	Angle from metadata
LED decay	$\gamma \text{ [s}^{-1}\text{]}$	$\gamma = \beta_{\text{fit}}$	First-order; α unused
Torricelli	k	$k = \alpha_{\text{fit}}$	Nonlinear Torricelli block

Temporal calibration. Δt is set to the inverse of the capture frame rate (60 fps $\rightarrow \Delta t = 1/60$ s for IRIS; Delfys75 uses $\Delta t = 0.05$ s). Mismatches between Δt and the true frame interval directly scale α and β by Δt^{-2} and Δt^{-1} respectively.

E VLM Prompting Strategies and Ablations

This appendix documents the exact prompt design and discusses additional strategies evaluated during development. See also the confusion matrix in Appendix E.5.

E.1 Frame Sampling

For all VLM calls, $m = 5$ representative frames are sampled at positions $\{0\%, 25\%, 50\%, 75\%, 100\%\}$ of the total duration. Earlier experiments used 3 frames and achieved $\sim 67\%$ accuracy; adding quartile frames increased accuracy to 73%.

E.2 Temporal Reasoning (Primary Variant)

The VLM receives the 5 sampled frames and a system-level prompt instructing it to *compare early and late frames* to resolve temporal ambiguity. The key design choice is the temporal-comparison instruction, which accounts for most of the accuracy gain from $\sim 61\%$ to 73% on Delfys75.

E.3 Describe-Then-Classify (Two-Call Variant)

This variant uses two sequential API calls: a description call (free text, no labels) followed by a classification call (text only, no images). On Delfys75, this achieved 61.11% accuracy. The dominant failure is `free.fall` (0% per-class accuracy): the description step produces ambiguous text that the classification step maps to `pendulum`.

Reversal on IRIS. The ranking reverses on IRIS: describe-then-classify achieves 72.92% while temporal reasoning drops to 65.00%. The two-stage pipeline allows the VLM to articulate complex dynamics (collisions, coupled oscillations) in free-form language, producing richer intermediate representations. The single-call temporal reasoning prompt, designed around six Delfys75 classes, struggles with IRIS’s novel motion patterns.

E.4 Additional Strategies Evaluated

Chain-of-thought (CoT). Accuracy $\sim 65\%$, lower than temporal reasoning, with higher token cost.

Few-shot prompting. Improved robustness for visually similar classes but impractical due to context length limits.

Self-consistency. Majority vote over $k = 5$ samples improved stability without meaningful accuracy gain.

VLM fine-tuning. LoRA fine-tuning collapsed to predicting a single class ($\sim 16.7\%$ accuracy) due to small dataset size. Not used in any reported result.

Video classifier (ResNet-18). Trained separately on each benchmark: 98.40% on Delfys75, 99.30% on IRIS. Near-perfect in-distribution but requires retraining for new phenomena.

E.5 VLM Confusion Matrices

Table S4 shows the confusion matrix for temporal-reasoning VLM on Delfys75. The primary failure is free_fall being predicted as pendulum (10/15): a ball shrinking in apparent size is visually indistinguishable from an object receding in oscillatory motion when only 5 frames are shown without metric scale context.

Table S4: **Confusion matrix, temporal-reasoning VLM on Delfys75.** Rows = ground truth, columns = predicted. Diagonal = correct.

	drop.	free	led	pend.	slide	torr.	Σ
dropped_ball	10	5	0	0	0	0	15
free_fall	0	0	0	10	5	0	15
led	0	0	15	0	0	0	15
pendulum	2	2	0	11	0	0	15
sliding_block	0	0	0	0	15	0	15
torricelli	0	0	0	0	0	15	15
Acc	66/90 = 73.3%						

F Implementation Details

F.1 Encoder Architecture

The encoder ϕ is a lightweight MLP operating on per-frame pixel intensities. Input frames are resized to 56×100 (grayscale) and flattened to a 5600-dimensional vector. The MLP has two hidden layers of 256 units each with ReLU activations, outputting $d = 2$ (mean μ_z and log-variance $\log \sigma_z^2$ for VAE reparameterisation). For multi-object phenomena, the encoder outputs $2N$ values, reshaped to $N \times 2$ per frame.

F.2 Physics Block

Each ODE family has a dedicated physics block with learnable scalars $\gamma = (\gamma_0, \gamma_1)$ initialised to $(0.5, 0.05)$. The discrete Euler-Cromer step is:

$$\dot{z}_{t+1} = \dot{z}_t + \Delta t \cdot \ddot{z}_t, \quad (\text{S1})$$

$$z_{t+1} = z_t + \Delta t \cdot \dot{z}_t + \Delta t^2 \cdot \ddot{z}_t, \quad (\text{S2})$$

where $\ddot{z}_t = -\gamma_1 \dot{z}_t - \gamma_0 z_t$. The critical fix is the $\Delta t^2 \cdot \ddot{z}_t$ term: without it, $\partial z_{t+1} / \partial \gamma = 0$ and physics parameters receive no gradient signal.

F.3 Training

Each clip is trained independently with Adam. Hyperparameters: learning rate 10^{-3} for the encoder, 10^{-2} for γ ; batch size = all temporal windows of the clip; 500 epochs; $\lambda_{\text{KL}} = 0.01$. All runs use seed = 42.

G Full IRIS Parameter Estimation Results

Table S5 reports parameter MAE on IRIS comparing one-step loss and multi-step rollout loss ($K=5$), both with the corrected Euler integrator and path-based equation selection.

Table S5: **Parameter MAE on IRIS: 1-step vs. multi-step loss.** $\Delta = \text{MAE}_{\text{multi}} - \text{MAE}_{\text{1-step}}$; negative = multi-step wins. Green = lower MAE; red = catastrophic ($|\Delta| > 10$).

Dynamics	Setting	Param	GT	1-step	Multi.	Δ
<i>Single-body</i>						
Dropping ball	drop.50	g [m/s ²]	9.81	1.04	6.88	+5.84
	drop.100	g [m/s ²]	9.81	2.26	8.28	+6.02
	drop.150	g [m/s ²]	9.81	3.83	8.86	+5.04
Falling ball	big	g [m/s ²]	9.81	4.26	6.40	+2.14
	mid	g [m/s ²]	9.81	6.63	8.63	+2.01
	small	g [m/s ²]	9.81	4.13	6.88	+2.74
Pendulum	pend._20	L [m]	0.50	0.56	0.40	-0.16
	pend._45	L [m]	0.50	0.34	1.16	+0.82
	pend._90	L [m]	0.50	0.60	21.95	+21.34
Rotation	fast	α	0.10	1.54	2.46	-0.64
		β	0.08	0.88	1.28	+0.39
	mid	α	0.10	3.03	3.98	-1.21
		β	0.05	0.39	1.38	+0.99
	slow	α	0.10	1.59	4.63	-2.11
		β	0.03	0.45	0.06	-0.39
Sliding cone	cone.45	α [deg]	45.0	0.00	0.00	0.00
	cone.60	α [deg]	60.0	0.00	0.00	0.00
	cone.80	α [deg]	80.0	0.00	0.00	0.00
<i>Multi-body</i>						
Two mov. pendulums	pend._20	L_1, L_2 [m]	0.50	1.14	741.1	+740.0
	pend._45	L_1, L_2 [m]	0.50	1.63	164.1	+162.5
	pend._90	L_1, L_2 [m]	0.50	3.01	149.9	+146.9
One stat. pendulum	pend._20	L_1, L_2 [m]	0.50	1.38	65.4	+64.0
	pend._45	L_1, L_2 [m]	0.50	0.77	96.8	+96.0
	pend._90	L_1, L_2 [m]	0.50	1.06	164.8	+163.8

Key observations. (1) Sliding cone angle is recovered exactly because it is taken from setting metadata. (2) Gravity (dropping/falling ball): the 1-step variant outperforms multi-step consistently. (3) Pendulum pend._90: catastrophic multi-step failure ($\Delta = +21.34$) reflects large-angle nonlinearity (Appendix J). (4) Multi-body pendulums: both variants yield large absolute errors due to the simplified contact model (Appendix H). (5) Hitting cones is excluded because κ has no independently measured ground-truth value.

H Multi-Body Contact Modeling: Details and Limitations

The graph-structured physics block models inter-object forces via a learnable spring-like coupling term $\kappa_{ij}(z_i - z_j)$ (main paper, Eq. 1). This is a deliberate simplification: (a) the architecture reduces to the single-body ODE when $N = 1$; (b) the coupling term is differentiable.

Known limitations. Real impacts involve restitution (velocity reversal), finite contact duration (the spring model spreads force over a continuous window), and friction at contact (not modelled). The fitted κ_{ij} is an *effective* coupling coefficient that conflates these effects into a single linear term.

Identifiability note. The coupling parameter κ_{ij} is only observable during the brief contact interval (≤ 1 s out of 6–20 s clips). The latent loss over the full clip is dominated by the non-contact phase, explaining the large MAE values. Future work should consider contact-segmented training windows or event-conditioned physics blocks.

I Identifiability Analysis

I.1 Gradient Norms

Without the Euler fix, γ_0 and γ_1 remain at their initial values for all 500 epochs; gradient norms are $< 10^{-8}$. After the fix, gradient norms are $\|\nabla_{\gamma}\mathcal{L}\|_2 \approx 0.3\text{--}1.5$ at epoch 1, decaying to $\approx 0.05\text{--}0.2$ at convergence.

I.2 Estimate Variance Across Trials

Table S6: **Estimate variance across 10 trials per IRIS setting.** Low σ indicates stable convergence; high σ indicates identifiability difficulties.

Dynamics	Setting	Param	GT	$\bar{\gamma}$	σ
Dropping ball	drop_50	g	9.81	8.77	0.42
Dropping ball	drop_100	g	9.81	7.55	1.21
Dropping ball	drop_150	g	9.81	5.98	2.04
Pendulum	pend._20	L [m]	0.50	1.06	0.88
Pendulum	pend._45	L [m]	0.50	0.84	0.41
Pendulum	pend._90	L [m]	0.50	1.10	0.73
Sliding cone	cone_45	α [deg]	45.0	45.0	0.00
Rotation	slow	β	0.03	0.48	0.09

Observations. (1) Sliding cone angle is recovered perfectly ($\sigma = 0$). (2) Gravity estimates are stable for short drops ($\sigma = 0.42$) but increasingly variable for longer drops. (3) Pendulum length shows moderate variance, consistent with the challenge of disentangling $\gamma_0 = g/L$ from the encoder’s internal scale.

J Pendulum Amplitude–Period Analysis

The small-angle approximation $T = 2\pi\sqrt{L/g}$ introduces systematic bias for finite amplitudes. The exact period of a simple pendulum is:

$$T_{\text{exact}}(\theta_0) = 4\sqrt{\frac{L}{g}} K\left(\sin\frac{\theta_0}{2}\right), \quad (\text{S3})$$

where $K(\cdot)$ is the complete elliptic integral of the first kind. The relative period correction $\delta T/T = T_{\text{exact}}/T_{\text{small}} - 1$ grows with amplitude:

Table S7: **Period–amplitude correction** and its effect on recovered L . L_{small} uses the small-angle formula; $L_{\text{corrected}}$ applies the exact period.

θ_0 (deg)	$\delta T/T$ (%)	L_{small} (m)	$L_{\text{corrected}}$ (m)	L_{GT} (m)
20	0.38	0.50	0.50	0.50
45	1.68	0.52	0.50	0.50
90	5.17	0.55	0.50	0.50

At $\theta_0 = 20^\circ$, the correction is negligible ($\delta T/T < 0.4\%$). At $\theta_0 = 90^\circ$, the small-angle approximation overestimates L by $\sim 10\%$; applying the exact correction brings the estimate back to ground truth. For the pendulum ODE (main paper, Eq. 1 single-body case), note that the $\sin\theta$ nonlinearity is retained, so the ODE itself does not assume small angles; the approximation arises only in the period-based SI extraction of L . The evaluation toolkit provides both small-angle and corrected-period L estimates.

K Multi-Step Loss: Horizon Ablation

Table S8 reports MAE as a function of rollout horizon K on Delfys75 for representative phenomena. $K=5$ achieves the lowest MAE for gravity-dominated phenomena (dropped ball, free fall), consistent with the identifiability argument. LED and Torricelli degrade at $K>3$ due to gradient instability in stiff exponential/square-root dynamics. On IRIS multi-body scenarios, catastrophic divergence occurs at all $K > 1$.

Table S8: **Multi-step horizon ablation on Delfys75**. MAE for selected (phenomenon, parameter) as a function of rollout horizon K .

Phenomenon	Param	$K=1$	$K=2$	$K=3$	$K=5$
Dropped ball	g (m/s ²)	0.25	0.22	0.20	0.18
Free fall (table)	g (m/s ²)	1.06	0.68	0.32	0.15
Pendulum (45)	L (m)	0.35	0.38	0.42	0.50
LED (10s)	γ	2.09	3.15	4.82	7.46
Torricelli (large)	k	6.27	6.31	6.42	6.54

L Integrator Comparison

Three integrators are compared on Delfys75 with multi-step loss ($K=5$): corrected Euler, Störmer-Verlet, and RK4. Störmer-Verlet achieves the lowest ODE residual and variance on conservative systems (pendulum, rotation) with negligible wall-clock overhead. RK4 provides marginally lower residual but at $\sim 4\times$ the computational cost. For non-conservative systems (LED, Torricelli), all three yield comparable MAE.

Table S9: **Integrator comparison on Delfys75** (multi-step loss, $K=5$). \mathcal{R} = ODE residual ($\times 10^{-3}$).

Phenom.	Param	Corrected Euler			Störmer-Verlet		
		MAE	σ	\mathcal{R}	MAE	σ	\mathcal{R}
Pendulum	L (m)	0.50	0.41	0.83	0.42	0.35	0.51
Free fall	g (m/s ²)	0.15	0.08	1.92	0.18	0.09	1.85
LED	γ	7.46	2.1	0.12	7.41	2.0	0.11
Rotation	α	3.98	1.5	0.41	3.62	1.3	0.28